Engineering Notes

Nonlinear Optimal Approach to Spacecraft Attitude Control Using Magnetic and Impulsive Actuations

Esmaeil Sharifi* and Christopher J. Damaren†
University of Toronto, Toronto, Ontario M3H 5T6, Canada

https://doi.org/10.2514/1.G004913

Nomenclature

$\boldsymbol{C}$	=	nonlinear control gain vector
J	=	hybrid performance index
$\boldsymbol{m}$	=	magnetic dipole moment vector, A · m^2
$\boldsymbol{u}$	=	control input
$\boldsymbol{x}$	=	state vector
$\boldsymbol{\varepsilon}$	=	vector part of quaternions
η	=	scalar part of quaternions
$\boldsymbol{\tau}$	=	torque vector, N · m
$\boldsymbol{\Phi}$	=	basis functions
$\boldsymbol{\omega}$	=	angular velocity vector, rad/s

Subscripts

b	=	expressed in body-fixed reference frame
ct	=	continuous-time variable
ds	=	discrete-time variable
i	=	expressed in inertial reference frame
imp	=	impulsive quantity
mag	=	magnetic quantity

I. Introduction

MAGNETIC torques originating from the interaction between the Earth's magnetic field and the onboard electromagnetic dipole moments can be used as an actuation mechanism for attitude control purposes [1–3]. In this regard, spacecraft operating in low Earth orbits (LEOs) can be equipped with three mutually perpendicular magnetic torquers. The most basic source of a magnetic torquer is a current loop; a planar loop of area $\mathcal{A}$ with $\mathcal{N}$ turns of wire carrying a current of $\mathcal{I}$ A produces a magnetic dipole moment of magnitude $\mathcal{N}\mathcal{I}\mathcal{A}$ in the direction normal to the plane of the loop, satisfying a right-hand rule [3]. Although this relation has the advantage of being a linear function of the current, sufficiently large quantities for $\mathcal{A}$ and $\mathcal{N}$ are necessary to produce the onboard dipole moments required by many spacecraft. For this reason, torque rods (which are coils of wire wrapped around ferromagnetic cores) are employed in practice to obtain greater dipole moments for a given amount of current [3]. Because the magnitude of the Earth's magnetic field decreases as the inverse cube of the distance from the center of the Earth, magnetic control torques are used almost exclusively in near-Earth orbits wherein the magnitude of the Earth's magnetic field is roughly in the range of 20–50 μT [3]. As a consequence, the control torques generated by magnetic actuation are typically on the order of 10^{-5} to 10^{-4} N · m for LEOs, depending on factors like orbit inclination [3].

Magnetic control torques are typically used for the detumbling [4] and momentum dumping [5,6] of spacecraft. In the former, the magnetic attitude control system detumbles the spacecraft immediately after launch by damping all angular velocity components of the spacecraft to zero; whereas in the latter, the primary task of the attitude control system is to dump excess wheel angular momentum induced by external disturbances [2,3]. Other applications of magnetic torquers include initial acquisition, precession control, nutation damping, and momentum control [3].

Attitude control using magnetic torques was first proposed in Ref. [7] in the 1960s, and then in Ref. [8] by developing the so-called B-dot control law for spacecraft detumbling and initial acquisition. A great deal of research has been devoted to the use of magnetic torques for both attitude control and momentum dumping thereafter. The early research was focused on approximating the time-varying behavior of magnetic actuators with its time-invariant equivalence assuming sufficiently slow closed-loop dynamics [9,10]. Periodic change in the properties of the geomagnetic field relative to spacecraft (as they orbit the Earth) has also inspired many researchers to employ a linear optimal control policy (time-varying, periodic, and constant gains) to stabilize the rotational dynamics of spacecraft [11–13]. For instance, Ref. [11] proposed an infinite-time horizon periodic attitude controller, wherein the geomagnetic field was averaged over a certain time interval to consider the periodic nature of the problem, and a finite-time horizon periodic controller, which incorporated the time history of the real geomagnetic field into the controller architecture. Lyapunov-based nonlinear techniques were also under investigation for magnetic attitude control [14,15]; in this regard, the periodicity of the Earth's magnetic field was used to apply the Krasovski–LaSalle theorem for the stability analysis. A survey of magnetic spacecraft attitude control using both linear and nonlinear design methods can be found in Ref. [16].

Magnetic attitude control systems possess several advantages for near-Earth missions, including 1) an essentially unlimited mission life due to use of a renewable source of actuation, 2) the absence of catastrophic failure modes, 3) the smoothness of application, 4) the possibility of smoothly modulating the control torque without inducing undesired coupling with flexible modes, and 5) significant savings in the overall weight and complexity of the system as compared to any other class of actuators owing to the absence of moving parts or plumbing [3,4,8].

On the other hand, as the main drawback associated with magnetic attitude control systems, magnetic torques are constrained to lie in the plane orthogonal to the magnetic field (due to the crossproduct between the onboard magnetic dipole moments and the magnetic field from which they originate); consequently, only two out of three axes can be controlled at a given time instant [3]. Moreover, controllability in such systems depends on orbit characteristics and the location of the spacecraft within the orbit [2]. However, full three-axis control for magnetic attitude control systems can be achieved over a complete orbit, provided that the spacecraft's orbital plane excludes the geomagnetic equatorial plane and the magnetic poles [17]. Another disadvantage related to magnetic attitude control is that moderately fast attitude maneuvers are almost limited to low-orbit missions [2].

To resolve the drawbacks inherently associated with magnetic actuation (namely, instantaneous underactuation and gain limitations), magnetic attitude control systems have been employed in conjunction

Received 25 October 2019; revision received 30 January 2020; accepted for publication 30 January 2020; published online 27 February 2020.

*Ph.D. Candidate, Spacecraft Dynamics and Control Laboratory, Institute for Aerospace Studies. Student Member AIAA.

†Professor and Director, Institute for Aerospace Studies. Associate Fellow AIAA.

with other forms of attitude control, from passive to active. Spin stabilization (Ref. [1] Secs. 19.1 and 19.2, and Refs. [18,19]) and gravity-gradient stabilization [9,10,14,15,20] are examples of passive control used collaboratively to support magnetic actuation, whereas reaction wheels [6,21–24] and thrusters [25,26] represent common techniques to actively complement magnetic control.

In this Note, nonlinear-based magnetic actuation is collaboratively augmented by impulsive thrusts for regulating the attitude motion of spacecraft. The main objective of this work is to extend the magnetic/impulsive spacecraft attitude control concept to a nonlinear optimal framework. By optimal combination of the magnetic torques and impulsive thrusts proposed in this Note, the use of both magnetic and impulsive control torques is optimized. Furthermore, the feedback attitude controller required to regulate the attitude motion of spacecraft is designed using the full nonlinear kinematics and dynamics of the system. No linearization is involved, neither dynamic feedback linearization nor a priori linearization of the rotational equations of motion. This is particularly useful for attitude control systems that can involve large angle slewing maneuvers (whereupon linear approximation is invalid), and nonlinear controllers are therefore required to appropriately compensate for the nonlinearities involved in the system. Using the proposed hybrid nonlinear optimal controller, not only are the uncontrollability issues and gain limitations inherently associated with magnetically actuated attitude control systems resolved but the performance of the system is also significantly improved as compared to linear-based controllers. Moreover, the magnetic attitude control can be applied to low inclined orbits in addition to high inclined ones, and global asymptotic stability can be achieved from a practical perspective.

This Note is organized as follows. The hybrid nonlinear optimal control framework recently proposed in Ref. [27] is briefly described in Sec. II. The kinematic and dynamic equations of motion characterizing the cascade nature of the spacecraft attitude motion are then reviewed in Sec. III. The algorithm developed in Sec. II is subsequently applied to the magnetic/impulsive attitude control problem in Sec. IV.

II. Control Approach

This section serves to develop an optimal control design framework for hybrid nonlinear dynamical systems that involve an interacting mixture of continuous-time and discrete-time dynamics. Such systems possess multiple modes of operation, and hence consist of three main elements: a set of differential equations, which characterizes the motion of the system between impulsive events; a set of difference equations, which governs instantaneous changes in the system states when an impulse occurs; and a criterion to determine when impulses are to be applied. Consider a hybrid system modeled by equations of the form

$$\begin{cases} \dot{\boldsymbol{x}}(t) = \boldsymbol{f}(\boldsymbol{x},t) + \boldsymbol{g}(\boldsymbol{x},t)\boldsymbol{u}_{\mathrm{ct}}(\boldsymbol{x},t), \boldsymbol{x}(\boldsymbol{0}) = \boldsymbol{x}_0 & t \neq t_k \\ \Delta\boldsymbol{x}(t_k) = \boldsymbol{x}(t_k^+) - \boldsymbol{x}(t_k^-) = \boldsymbol{B}_{\mathrm{ds}}\boldsymbol{u}_{\mathrm{ds},k} & t = t_k \end{cases} \tag{1}$$

where $x \in \mathcal{D} \subseteq \mathbb{R}^n$ is the state vector; $\mathcal{D}$ specifies an open set with $\boldsymbol{0} \in \mathcal{D}$; $\boldsymbol{f}:\mathcal{D}\times\mathbb{R} \to \mathbb{R}^n$ and $\boldsymbol{g}:\mathcal{D}\times\mathbb{R} \to \mathbb{R}^{n\times m_{\mathrm{ct}}}$ are assumed to be Lipschitz continuous on $\mathcal{D}$; t_k denotes the time instants at which impulses are to be applied; $\boldsymbol{x}(t_k^-)$ and $\boldsymbol{x}(t_k^+)$ are, respectively, the state vectors immediately before and after the discrete-time dynamics are applied at $t = t_k$; $\boldsymbol{u}_{\mathrm{ds}}(\boldsymbol{x}(t_k), t_k) \triangleq \boldsymbol{u}_{\mathrm{ds},k}$; $(\boldsymbol{u}_{\mathrm{ct}}, \boldsymbol{u}_{\mathrm{ds},k}) \in \boldsymbol{U}_{\mathrm{ct}} \times \boldsymbol{U}_{\mathrm{ds}} \subseteq \mathbb{R}^{m_{\mathrm{ct}}} \times \mathbb{R}^{m_{\mathrm{ds}}}$ is the hybrid control input with $t \in [t_0, t_f]$ and $k \in \mathbb{Z}_{(t_0,t_f)}$; and $\boldsymbol{B}_{\mathrm{ds}} \in \mathbb{R}^{n\times m_{\mathrm{ds}}}$ indicates the discrete-time control input matrix. It is also assumed that $(\boldsymbol{u}_{\mathrm{ct}}, \boldsymbol{u}_{\mathrm{ds},k})$ is restricted to the class of admissible controls $\mathcal{U}_{\mathrm{ct}} \times \mathcal{U}_{\mathrm{ds}}$ consisting of measurable functions $(\boldsymbol{u}_{\mathrm{ct}}, \boldsymbol{u}_{\mathrm{ds},k})$ such that $(\boldsymbol{u}_{\mathrm{ct}}, \boldsymbol{u}_{\mathrm{ds},k}) \in \boldsymbol{U}_{\mathrm{ct}} \times \boldsymbol{U}_{\mathrm{ds}}$, where the constraint set $\boldsymbol{U}_{\mathrm{ct}} \times \boldsymbol{U}_{\mathrm{ds}}$ is given with $(\boldsymbol{0}, \boldsymbol{0}) \in \boldsymbol{U}_{\mathrm{ct}} \times \boldsymbol{U}_{\mathrm{ds}}$. The main objective is therefore to determine a hybrid nonlinear control input $(\boldsymbol{u}_{\mathrm{ct}}, \boldsymbol{u}_{\mathrm{ds},k}) \in \boldsymbol{U}_{\mathrm{ct}} \times \boldsymbol{U}_{\mathrm{ds}}$, $t \in [t_0, t_f]$ and $k \in \mathbb{Z}_{(t_0,t_f)}$, such that the following hybrid performance index is minimized over all admissible control inputs $(\boldsymbol{u}_{\mathrm{ct}}, \boldsymbol{u}_{\mathrm{ds},k}) \in \mathcal{U}_{\mathrm{ct}} \times \mathcal{U}_{\mathrm{ds}}$ [28]:

$$J(\boldsymbol{x}_0, \boldsymbol{u}_{\mathrm{ct}}, \boldsymbol{u}_{\mathrm{ds},k}, t_0) = \int_{t_0}^{t_f} L_{\mathrm{ct}}(\boldsymbol{x}(t), \boldsymbol{u}_{\mathrm{ct}}(t), t)\,\mathrm{d}t + \sum_{k=1}^{N_{\mathrm{imp}}} L_{\mathrm{ds}}(\boldsymbol{x}(t_k), \boldsymbol{u}_{\mathrm{ds},k}, t_k) \tag{2}$$

where $L_{\mathrm{ct}}:\mathcal{D}\times\boldsymbol{U}_{\mathrm{ct}}\times\mathbb{R} \to \mathbb{R}$ and $L_{\mathrm{ds}}:\mathcal{D}\times\boldsymbol{U}_{\mathrm{ds}}\times\mathbb{R} \to \mathbb{R}$ are, respectively, the continuous-time and discrete-time instantaneous cost functions; and N_{imp} specifies the number of impulses during the operating time. Whereas the necessary and sufficient conditions for minimizing this hybrid performance index, given a hybrid control input $(\boldsymbol{u}_{\mathrm{ct}}, \boldsymbol{u}_{\mathrm{ds},k})$, are obtained via a hybrid version of Bellman's principle of optimality [28], the asymptotic stability of the hybrid nonlinear closed-loop system can be guaranteed by relating the hybrid performance index [Eq. (2)] to an underlying Lyapunov function in a specific way [28]. This Lyapunov function can be shown to be a solution of the hybrid Hamilton–Jacobi–Bellman (HJB) equation shown in the following, thereby guaranteeing both optimality and asymptotic stability of the hybrid feedback control system (see Refs. [27,28] for a detailed discussion):

$$\frac{\partial V(\boldsymbol{x},t)}{\partial t} + \min_{\boldsymbol{u}_{\mathrm{ct}} \in \mathcal{U}_{\mathrm{ct}}} \{\mathcal{H}_{\mathrm{ct}}(\boldsymbol{x}, \boldsymbol{u}_{\mathrm{ct}}, \partial V(\boldsymbol{x},t)/\partial \boldsymbol{x}, t)\} = 0 \qquad t \neq t_k \tag{3}$$

$$\min_{\boldsymbol{u}_{\mathrm{ds},k} \in \mathcal{U}_{\mathrm{ds}}} \{\mathcal{H}_{\mathrm{ds}}(\boldsymbol{x}, \boldsymbol{u}_{\mathrm{ds},k}, V(\boldsymbol{x}, t_k), t_k)\} = 0 \qquad t = t_k \tag{4}$$

where $V:\mathcal{D}\times\mathbb{R} \to \mathbb{R}$ denotes a continuously differentiable positive-definite function called the value function (the optimum value of the performance index); and $\mathcal{H}_{\mathrm{ct}}$ and $\mathcal{H}_{\mathrm{ds}}$ define, respectively, the Hamiltonians associated with the continuous-time and discrete-time dynamics as follows [28]:

$$\mathcal{H}_{\mathrm{ct}}(\boldsymbol{x}, \boldsymbol{u}_{\mathrm{ct}}, \partial V/\partial \boldsymbol{x}, t) \triangleq L_{\mathrm{ct}}(\boldsymbol{x}, \boldsymbol{u}_{\mathrm{ct}}, t) + (\partial V(\boldsymbol{x},t)/\partial \boldsymbol{x})^{\mathrm{T}}(\boldsymbol{f}(\boldsymbol{x},t) + \boldsymbol{g}(\boldsymbol{x},t)\boldsymbol{u}_{\mathrm{ct}}(\boldsymbol{x},t)) \tag{5}$$

$$\mathcal{H}_{\mathrm{ds}}(\boldsymbol{x}, \boldsymbol{u}_{\mathrm{ds},k}, V(\boldsymbol{x}, t_k), t_k) \triangleq L_{\mathrm{ds}}(\boldsymbol{x}_k^-, \boldsymbol{u}_{\mathrm{ds},k}, t_k) + V(\boldsymbol{x}_k^+, t_k^+) - V(\boldsymbol{x}_k^-, t_k^-) \tag{6}$$

wherein $\boldsymbol{x}_k^{\pm} \triangleq \boldsymbol{x}(t_k^{\pm})$ and $V(\boldsymbol{x}_k^+, t_k^+) = V(\boldsymbol{x}_k^- + \boldsymbol{B}_{\mathrm{ds}}\boldsymbol{u}_{\mathrm{ds},k}, t_k^+)$. From optimal control theory, it is well known that the nonlinear optimal control depends on the solution to the HJB equation, which is generally difficult to solve; hence, approximation techniques are necessitated. Two numerical approaches are therefore employed in the following subsections to approximate the continuous-time and discrete-time portions of the hybrid HJB equation, respectively. The Galerkin spectral method [29] is used in Sec. II.A to derive a set of differential equations through which the optimal control gains are computed between impulsive events. Employing the spectral collocation method (Ref. [30] Chap. 12), a set of algebraic equations is then developed in Sec. II.B to find the optimal control gain vector at impulsive instants. These two algorithms are ultimately combined in Sec. II.C to obtain the hybrid nonlinear optimal control law for attitude control purposes. The reader is referred to Ref. [27] for a detailed discussion on the proposed hybrid nonlinear optimal control architecture.

A. Numerical Solution to the Continuous-Time HJB Equation

Applying the Galerkin spectral method directly to the continuous-time HJB equation, a set of differential equations is derived in this section to compute the time-varying optimal control gains between impulsive instants. Defining

$$L_{\mathrm{ct}}(\boldsymbol{x}, \boldsymbol{u}_{\mathrm{ct}}, t) = l_{\mathrm{ct}}(\boldsymbol{x}) + \|\boldsymbol{u}_{\mathrm{ct}}(\boldsymbol{x},t)\|^2_{\boldsymbol{R}_{\mathrm{ct}}}$$

where $l_{\mathrm{ct}}:\mathcal{D} \to \mathbb{R}$ is a positive-definite function called the continuous-time state penalty function and $\boldsymbol{R}_{\mathrm{ct}} \in \mathbb{R}^{m_{\mathrm{ct}}\times m_{\mathrm{ct}}}$ denotes a symmetric positive-definite matrix called the continuous-time control penalty matrix, the continuous-time optimal control law in terms of

$V(\boldsymbol{x}, t)$ can be found by minimizing Eq. (3) with respect to $\boldsymbol{u}_{\text{ct}}$ as follows (Ref. [31] Chap. 6):

$$\boldsymbol{u}^*_{\text{ct}}(\boldsymbol{x}, t) = -\frac{1}{2}\boldsymbol{R}^{-1}_{\text{ct}}\boldsymbol{g}^{\text{T}}(\boldsymbol{x}, t)\frac{\partial V(\boldsymbol{x}, t)}{\partial \boldsymbol{x}} \tag{7}$$

By substituting Eq. (7) into Eq. (3), the continuous-time HJB equation can be thus formulated as

$$\begin{cases} \text{HJB}_{\text{ct}}(V) = \frac{\partial V}{\partial t} + \left(\frac{\partial V}{\partial \boldsymbol{x}}\right)^{\text{T}}\boldsymbol{f} - \frac{1}{4}\left(\frac{\partial V}{\partial \boldsymbol{x}}\right)^{\text{T}}\boldsymbol{g}\boldsymbol{R}^{-1}_{\text{ct}}\boldsymbol{g}^{\text{T}}\frac{\partial V}{\partial \boldsymbol{x}} + l_{\text{ct}} = 0 \\ V(\boldsymbol{x}_f, t_f) = 0 \end{cases} \tag{8}$$

where $\boldsymbol{x}_f \triangleq \boldsymbol{x}(t_f)$. The continuous-time HJB equation, as a nonlinear partial differential equation, is difficult to solve in general, thereby necessitating approximation techniques. The Galerkin spectral method can be therefore exploited to approximate the solution to Eq. (8). The basic idea underlying the Galerkin approach is to assume that the solution of the continuous-time HJB equation can be expressed as an infinite sum of known basis functions [32]. In addition, for the Galerkin method to be applicable, the problem must be placed in a suitable inner product space such that the projection is well defined in terms of n-dimensional integrations [32]. The approximation is thus restricted to a closed and bounded set in $\mathcal{D}$, namely, a compact set Ω, which defines the bounded domain of the state space of interest. Consequently, it is first assumed that the value function can be discretized by an infinite series of prescribed state-dependent basis functions, which are continuous and defined everywhere on Ω, and unknown coefficients with time dependency as follows [32]:

$$V(\boldsymbol{x}, t) \coloneqq \sum_{j=1}^{\infty} c^*_j(t)\phi_j(\boldsymbol{x}) \tag{9}$$

From a practical perspective, using an infinite number of terms in the discretization is impossible; the approximation for $V(\boldsymbol{x}, t)$ is therefore carried one step further by considering a truncated version of the infinite series:

$$V_N(\boldsymbol{x}, t) \coloneqq \sum_{j=1}^{N} c^*_j(t)\phi_j(\boldsymbol{x}) = \boldsymbol{\Phi}^{\text{T}}_N(\boldsymbol{x})\boldsymbol{C}^*_N(t) \tag{10}$$

wherein $\boldsymbol{\Phi}_N(\boldsymbol{x}) = [\phi_1, \ldots, \phi_N]^{\text{T}}$, $\boldsymbol{C}^*_N(t) = [c^*_1, \ldots, c^*_N]^{\text{T}}$, and N denotes the number of basis elements, i.e., the order of approximation. Using the Galerkin spectral method, the unknown coefficients $\boldsymbol{C}^*_N(t)$ can be determined by projecting the error, resulting from approximating the value function with $V_N(\boldsymbol{x}, t)$, onto the same basis functions retained in the truncated series (the linear finite basis spanned by $\{\phi_j\}^N_1$) and setting the outcome equal to zero:

$$\begin{cases} \langle \boldsymbol{\Phi}_N, \boldsymbol{\Phi}_N\rangle_\Omega \dot{\boldsymbol{C}}^*_N(t) + \langle \mathbf{J}_{\boldsymbol{x}}(\boldsymbol{\Phi}_N)\boldsymbol{f}, \boldsymbol{\Phi}_N\rangle_\Omega \boldsymbol{C}^*_N(t) \\ -\frac{1}{4}\left[\sum_{\text{k}=1}^{N} c^*_{\text{k}}(t)\left\langle \mathbf{J}_{\boldsymbol{x}}(\boldsymbol{\Phi}_N)\boldsymbol{g}\boldsymbol{R}^{-1}_{\text{ct}}\boldsymbol{g}^{\text{T}}\frac{\partial \phi_{\text{k}}}{\partial \boldsymbol{x}}, \boldsymbol{\Phi}_N\right\rangle_\Omega\right]\boldsymbol{C}^*_N(t) + \langle l_{\text{ct}}, \boldsymbol{\Phi}_N\rangle_\Omega = \boldsymbol{0} \\ \langle \boldsymbol{\Phi}_N, \boldsymbol{\Phi}_N\rangle_\Omega \boldsymbol{C}^*_N(t_f) = \boldsymbol{0} \end{cases} \tag{11}$$

wherein the projection operator is the inner product

$$\langle (\cdot), \phi_i(\boldsymbol{x})\rangle_\Omega \triangleq \int_\Omega (\cdot)\phi_i(\boldsymbol{x})\,\text{d}\boldsymbol{x}$$

computed over Ω, and $\mathbf{J}_{\boldsymbol{x}}$ denotes the Jacobian operator (matrix) with respect to $\boldsymbol{x}$. Omitting the detail, the following set of nonlinear ordinary differential equations (termed the continuous-time optimal control gain equations) therefore needs to be solved for $\boldsymbol{C}^*_N(t)$ in order to find the continuous-time optimal control law, assuming the equations have no escape in finite time:

$$\dot{\boldsymbol{C}}^*_N(t) + \boldsymbol{A}(t, c^*_{\text{k}}(t))\boldsymbol{C}^*_N(t) + \boldsymbol{b} = \boldsymbol{0}, \qquad \boldsymbol{C}^*_N(t_f) = \boldsymbol{0} \tag{12}$$

where

$$\begin{aligned} \boldsymbol{M}(t, c^*_{\text{k}}(t)) &= \sum_{\text{k}=1}^{N} c^*_{\text{k}}(t)\left\langle \mathbf{J}_{\boldsymbol{x}}(\boldsymbol{\Phi}_N)\boldsymbol{g}\boldsymbol{R}^{-1}_{\text{ct}}\boldsymbol{g}^{\text{T}}\frac{\partial \phi_{\text{k}}}{\partial \boldsymbol{x}}, \boldsymbol{\Phi}_N\right\rangle_\Omega \\ \boldsymbol{A}(t, c^*_{\text{k}}(t)) &= \langle \boldsymbol{\Phi}_N, \boldsymbol{\Phi}_N\rangle^{-1}_\Omega\left[\langle \mathbf{J}_{\boldsymbol{x}}(\boldsymbol{\Phi}_N)\boldsymbol{f}, \boldsymbol{\Phi}_N\rangle_\Omega - \frac{1}{4}\boldsymbol{M}(t, c^*_{\text{k}}(t))\right] \\ \boldsymbol{b} &= \langle \boldsymbol{\Phi}_N, \boldsymbol{\Phi}_N\rangle^{-1}_\Omega\langle l_{\text{ct}}, \boldsymbol{\Phi}_N\rangle_\Omega \end{aligned} \tag{13}$$

Once the optimal control gains $\boldsymbol{C}^*_N(t)$ are computed via backward integration of Eq. (12), the continuous-time optimal control law can be obtained by

$$\boldsymbol{u}^*_{\text{ct}}(\boldsymbol{x}, t) = -\frac{1}{2}\boldsymbol{R}^{-1}_{\text{ct}}\boldsymbol{g}^{\text{T}}(\boldsymbol{x}, t)\mathbf{J}^{\text{T}}_{\boldsymbol{x}}(\boldsymbol{\Phi}_N(\boldsymbol{x}))\boldsymbol{C}^*_N(t) \tag{14}$$

B. Numerical Solution to the Discrete-Time HJB Equation

With the continuous-time optimal control gain equations [Eq. (12)] thus derived, a set of algebraic equations is developed in this section to compute the optimal control gain vector associated with each jump at $t = t_k$ (see Ref. [27] for a detailed discussion). Defining

$$L_{\text{ds}}(\boldsymbol{x}^-_k, \boldsymbol{u}_{\text{ds},k}, t_k) = l_{\text{ds}}(\boldsymbol{x}^-_k) + \|\boldsymbol{u}_{\text{ds},k}\|^2_{\boldsymbol{R}_{\text{ds}}}$$

wherein $l_{\text{ds}}: \mathcal{D} \to \mathbb{R}$ is the discrete-time state penalty function and $\boldsymbol{R}_{\text{ds}} \in \mathbb{R}^{m_{\text{ds}} \times m_{\text{ds}}}$ denotes a symmetric positive-definite matrix called the discrete-time control penalty matrix, the discrete-time optimal control law can be then found by minimizing Eq. (4) with respect to $\boldsymbol{u}_{\text{ds},k}$:

$$\boldsymbol{u}^*_{\text{ds},k} = -\frac{1}{2}\boldsymbol{R}^{-1}_{\text{ds}}\boldsymbol{B}^{\text{T}}_{\text{ds}}\frac{\partial V(\boldsymbol{x}^+_k, t^+_k)}{\partial \boldsymbol{x}} = -\frac{1}{2}\boldsymbol{R}^{-1}_{\text{ds}}\boldsymbol{B}^{\text{T}}_{\text{ds}}\frac{\partial V(\boldsymbol{x}^-_k + \boldsymbol{B}_{\text{ds}}\boldsymbol{u}^*_{\text{ds},k}, t^+_k)}{\partial \boldsymbol{x}} \tag{15}$$

Substituting Eq. (15) into the discrete-time HJB equation along with use of the truncated version of the discretized value function [Eq. (10)] yields the following set of algebraic equations at each jump instant ($t = t_k$):

$$\begin{aligned} l_{\text{ds}}(\boldsymbol{x}^-_k) &+ \frac{1}{4}[\mathbf{J}^{\text{T}}_{\boldsymbol{x}}(\boldsymbol{\Phi}_N(\boldsymbol{x}))|_{\boldsymbol{x}=\boldsymbol{x}^-_k+\boldsymbol{B}_{\text{ds}}\boldsymbol{u}^*_{\text{ds},k}}\boldsymbol{C}^*_N(t^+_k)]^{\text{T}} \\ &\times \boldsymbol{B}_{\text{ds}}\boldsymbol{R}^{-1}_{\text{ds}}\boldsymbol{B}^{\text{T}}_{\text{ds}}[\mathbf{J}^{\text{T}}_{\boldsymbol{x}}(\boldsymbol{\Phi}_N(\boldsymbol{x}))|_{\boldsymbol{x}=\boldsymbol{x}^-_k+\boldsymbol{B}_{\text{ds}}\boldsymbol{u}^*_{\text{ds},k}}\boldsymbol{C}^*_N(t^+_k)] \\ &+ \boldsymbol{\Phi}^{\text{T}}_N(\boldsymbol{x}^-_k + \boldsymbol{B}_{\text{ds}}\boldsymbol{u}^*_{\text{ds},k})\boldsymbol{C}^*_N(t^+_k) - \boldsymbol{\Phi}^{\text{T}}_N(\boldsymbol{x}^-_k)\boldsymbol{C}^*_N(t^-_k) = 0 \end{aligned} \tag{16}$$

$\boldsymbol{C}^*_N(t^-_k)$ can be therefore computed through the preceding set of equations with $\boldsymbol{C}^*_N(t^+_k)$ available from the backward integration of Eq. (12). To this end, the following function is first defined substituting Eq. (10) into Eq. (15) and then rearranging the resulting equation] in terms of $\boldsymbol{u}^*_{\text{ds},k}$ and $\boldsymbol{x}^-_k$ with known quantities $c^*_j(t^+_k)$ to be solved for $\boldsymbol{u}^*_{\text{ds},k}$:

$$\boldsymbol{F}(\boldsymbol{u}^*_{\text{ds},k}) = 2\boldsymbol{R}_{\text{ds}}\boldsymbol{u}^*_{\text{ds},k} + \boldsymbol{B}^{\text{T}}_{\text{ds}}\sum_{j=1}^{N} c^*_j(t^+_k)\frac{\partial \phi_j(\boldsymbol{x}^-_k + \boldsymbol{B}_{\text{ds}}\boldsymbol{u}^*_{\text{ds},k})}{\partial \boldsymbol{x}} = \boldsymbol{0} \tag{17}$$

Newton's method [30] is then used to iteratively solve the equation $\boldsymbol{F}(\boldsymbol{u}^*_{\text{ds},k}) = \boldsymbol{0}$ for $\boldsymbol{u}^{*(i+1)}_{\text{ds},k}$, starting with $\boldsymbol{u}^{*(i)}_{\text{ds},k}$:

$$\boldsymbol{u}^{*(i+1)}_{\text{ds},k} = \boldsymbol{u}^{*(i)}_{\text{ds},k} - \left(\frac{\partial \boldsymbol{F}(\boldsymbol{u}^{*(i)}_{\text{ds},k})}{\partial \boldsymbol{u}^{*\text{T}}_{\text{ds},k}}\right)^{-1}\boldsymbol{F}(\boldsymbol{u}^{*(i)}_{\text{ds},k}) \tag{18}$$

Substituting Eq. (17) into Eq. (18) along with collocating $\boldsymbol{x}^-_k$ with a suitable set of points, $\bar{\boldsymbol{x}} = \underset{m}{row}\{\bar{\boldsymbol{x}}_m\}$, yields

Hybrid Nonlinear Optimal Control	*Hybrid Riccati-Based Optimal (LQR) Control*
$\begin{cases} \dot{\boldsymbol{x}} = \boldsymbol{f}(\boldsymbol{x},t) + \boldsymbol{g}(\boldsymbol{x},t)\boldsymbol{u}_{\text{ct}}(\boldsymbol{x},t) & t \neq t_{\text{k}} \\ \boldsymbol{x}_{\text{k}}^{+} = \boldsymbol{x}_{\text{k}}^{-} + \boldsymbol{B}_{\text{ds}}\boldsymbol{u}_{\text{ds,k}} & t = t_{\text{k}} \end{cases}, \ \boldsymbol{x}(\boldsymbol{0}) = \boldsymbol{x}_0$	$\begin{cases} \dot{\boldsymbol{x}} = \boldsymbol{A}_{\text{ct}}(t)\boldsymbol{x} + \boldsymbol{B}_{\text{ct}}(t)\boldsymbol{u}_{\text{ct}}(\boldsymbol{x},t) & t \neq t_{\text{k}} \\ \boldsymbol{x}_{\text{k}}^{+} = \boldsymbol{x}_{\text{k}}^{-} + \boldsymbol{B}_{\text{ds}}\boldsymbol{u}_{\text{ds,k}} & t = t_{\text{k}} \end{cases}, \ \boldsymbol{x}(\boldsymbol{0}) = \boldsymbol{x}_0$
$V_N(\boldsymbol{x},t) \coloneqq \sum_{j=1}^{N} c_j^*(t)\phi_j(\boldsymbol{x}) = \boldsymbol{\Phi}_N^{\text{T}}(\boldsymbol{x})\boldsymbol{C}_N^*(t)$	$V(\boldsymbol{x},t) \coloneqq \boldsymbol{x}^{\text{T}}\boldsymbol{P}(t)\boldsymbol{x}$
$J(\boldsymbol{x},\boldsymbol{u}_{\text{ct}},\boldsymbol{u}_{\text{ds,k}},t) = \int_{t_0}^{t_f}\left(l_{\text{ct}}(\boldsymbol{x}) + \lVert\boldsymbol{u}_{\text{ct}}\rVert_{\boldsymbol{R}_{\text{ct}}}^2\right)dt + \sum_{\text{k}=1}^{N_{imp}}\left(l_{\text{ds}}(\boldsymbol{x}_{\text{k}}^{-}) + \lVert\boldsymbol{u}_{\text{ds,k}}\rVert_{\boldsymbol{R}_{\text{ds}}}^2\right)$	$J(\boldsymbol{x},\boldsymbol{u}_{\text{ct}},\boldsymbol{u}_{\text{ds,k}},t) = \int_{t_0}^{t_f}(\boldsymbol{x}^{\text{T}}\boldsymbol{Q}_{\text{ct}}\boldsymbol{x} + \boldsymbol{u}_{\text{ct}}^{\text{T}}\boldsymbol{R}_{\text{ct}}\boldsymbol{u}_{\text{ct}})\,dt + \sum_{\text{k}=1}^{N_{imp}}(\boldsymbol{x}_{\text{k}}^{-\text{T}}\boldsymbol{Q}_{\text{ds}}\boldsymbol{x}_{\text{k}}^{-} + \boldsymbol{u}_{\text{ds,k}}^{\text{T}}\boldsymbol{R}_{\text{ds}}\boldsymbol{u}_{\text{ds,k}})$
$\begin{cases} \dot{\boldsymbol{C}}_N^*(t) + \boldsymbol{A}\left(t,c_{\text{k}}^*(t)\right)\boldsymbol{C}_N^*(t) + \boldsymbol{b} = \boldsymbol{0}\ ,\ \boldsymbol{C}_N^*(t_f) = \boldsymbol{0} & \\ \text{See Eq. (13)} & t \neq t_{\text{k}} \\ \boldsymbol{C}_N^*(t_{\text{k}}^{-}) = \left(\boldsymbol{\Psi}_{\text{k}}^{-}(\bar{\boldsymbol{x}})\right)^{-1}\left[\boldsymbol{W}_{\text{k}}(\bar{\boldsymbol{x}}) + \boldsymbol{\Psi}_{\text{k}}^{+}(\bar{\boldsymbol{x}})\boldsymbol{C}_N^*(t_{\text{k}}^{+})\right] & \\ \text{See Eq. (21)} & t = t_{\text{k}} \end{cases}$	$\begin{cases} \dot{\boldsymbol{P}}(t) + \boldsymbol{A}_{\text{ct}}^{\text{T}}\boldsymbol{P}(t) + \boldsymbol{P}(t)\boldsymbol{A}_{\text{ct}} + \boldsymbol{Q}_{\text{ct}} & \\ -\boldsymbol{P}(t)\boldsymbol{B}_{\text{ct}}\boldsymbol{R}_{\text{ct}}^{-1}\boldsymbol{B}_{\text{ct}}^{\text{T}}\boldsymbol{P}(t) = \boldsymbol{0}\ ,\ \boldsymbol{P}(t_f) = \boldsymbol{0} & t \neq t_{\text{k}} \\ \boldsymbol{P}_{\text{k}}^{-} = \boldsymbol{Q}_{\text{ds}} + \boldsymbol{P}_{\text{k}}^{+} & \\ \quad -\boldsymbol{P}_{\text{k}}^{+}\boldsymbol{B}_{\text{ds}}\left[\boldsymbol{R}_{\text{ds}} + \boldsymbol{B}_{\text{ds}}^{\text{T}}\boldsymbol{P}_{\text{k}}^{+}\boldsymbol{B}_{\text{ds}}\right]^{-1}\boldsymbol{B}_{\text{ds}}^{\text{T}}\boldsymbol{P}_{\text{k}}^{+} & t = t_{\text{k}} \end{cases}$
$\boldsymbol{C}_N^*(t)$	$\boldsymbol{P}(t)$
$\begin{cases} \boldsymbol{u}_{\text{ct}}^{*} = -\frac{1}{2}\boldsymbol{R}_{\text{ct}}^{-1}\boldsymbol{g}^{\text{T}}(\boldsymbol{x},t)\boldsymbol{\text{J}}_{\boldsymbol{x}}^{\text{T}}\left(\boldsymbol{\Phi}_N(\boldsymbol{x})\right)\boldsymbol{C}_N^*(t) & t \neq t_{\text{k}} \\ \boldsymbol{u}_{\text{ds,k}}^{*} = -\frac{1}{2}\boldsymbol{R}_{\text{ds}}^{-1}\boldsymbol{B}_{\text{ds}}^{\text{T}}\,\boldsymbol{\text{J}}_{\boldsymbol{x}}^{\text{T}}\left(\boldsymbol{\Phi}_N(\boldsymbol{x})\right)\big\rvert_{\boldsymbol{x}=\boldsymbol{x}_{\text{k}}^{+}}\boldsymbol{C}_N^*(t_{\text{k}}^{+}) & t = t_{\text{k}} \end{cases}$	$\begin{cases} \boldsymbol{u}_{\text{ct}}^{*} = -\boldsymbol{R}_{\text{ct}}^{-1}\boldsymbol{B}_{\text{ct}}^{\text{T}}(t)\boldsymbol{P}(t)\boldsymbol{x} & t \neq t_{\text{k}} \\ \boldsymbol{u}_{\text{ds,k}}^{*} = -\boldsymbol{R}_{\text{ds}}^{-1}\boldsymbol{B}_{\text{ds}}^{\text{T}}\left[\boldsymbol{P}_{\text{k}}^{-} - \boldsymbol{Q}_{\text{ds}}\right]\boldsymbol{x}_{\text{k}}^{-} & t = t_{\text{k}} \end{cases}$

Fig. 1 Comparison between hybrid nonlinear optimal control (left column) and hybrid LQR control (right column).

$$\boldsymbol{u}_{\text{ds},k}^{*(i+1)} = \boldsymbol{u}_{\text{ds},k}^{*(i)} - \left(2\boldsymbol{R}_{\text{ds}} + \boldsymbol{B}_{\text{ds}}^{\text{T}}\sum_{j=1}^{N} c_j^*(t_k^+)\mathbf{H}_{\boldsymbol{x}}(\phi_j(\boldsymbol{x}))|_{\boldsymbol{x}=\chi_{k,m}^+}\boldsymbol{B}_{\text{ds}}\right)^{-1} \times (2\boldsymbol{R}_{\text{ds}}\boldsymbol{u}_{\text{ds},k}^{*(i)} + \boldsymbol{B}_{\text{ds}}^{\text{T}}\mathbf{J}_{\boldsymbol{x}}^{\text{T}}(\boldsymbol{\Phi}_N(\boldsymbol{x}))|_{\boldsymbol{x}=\chi_{k,m}^+}\boldsymbol{C}_N^*(t_k^+)) \tag{19}$$

wherein $m = 1, \ldots, N$, $\chi_{k,m}^+ = \bar{\boldsymbol{x}}_m + \boldsymbol{B}_{\text{ds}}\boldsymbol{u}_{\text{ds},k}^{*(i)}$, and $\mathbf{H}_{\boldsymbol{x}}$ is the Hessian matrix with respect to $\boldsymbol{x}$. Initializing Eq. (19) with a suitable choice, the discrete-time optimal control corresponding to each $\bar{\boldsymbol{x}}_m$ at $t = t_k$, $\boldsymbol{u}_{\text{ds},k}^*(\bar{\boldsymbol{x}}_m, t_k)$, can therefore be computed. Using the spectral collocation method at each jump instant and substituting $\boldsymbol{u}_{\text{ds},k}^*(\bar{\boldsymbol{x}}_m, t_k)$ computed from Eq. (19) into Eq. (16), the discrete-time optimal control gain equations are obtained to be solved for $\boldsymbol{C}_N^*(t_k^-)$ as follows:

$$\boldsymbol{C}_N^*(t_k^-) = (\boldsymbol{\Psi}_k^-(\bar{\boldsymbol{x}}))^{-1}[\boldsymbol{W}_k(\bar{\boldsymbol{x}}) + \boldsymbol{\Psi}_k^+(\bar{\boldsymbol{x}})\boldsymbol{C}_N^*(t_k^+)] \tag{20}$$

where

$$\begin{aligned} \boldsymbol{\Upsilon}(\bar{\boldsymbol{x}}_m) &= \mathbf{J}_{\boldsymbol{x}}^{\text{T}}(\boldsymbol{\Phi}_N(\boldsymbol{x}))|_{\boldsymbol{x}=\bar{\boldsymbol{x}}_m + \boldsymbol{B}_{\text{ds}}\boldsymbol{u}_{\text{ds},k}^*(\bar{\boldsymbol{x}}_m, t_k)}\boldsymbol{C}_N^*(t_k^+) \\ \boldsymbol{W}_k(\bar{\boldsymbol{x}}) &= \underset{m}{\text{column}}\left\{l_{\text{ds}}(\bar{\boldsymbol{x}}_m) + \frac{1}{4}(\boldsymbol{\Upsilon}^{\text{T}}(\bar{\boldsymbol{x}}_m)\boldsymbol{B}_{\text{ds}}\boldsymbol{R}_{\text{ds}}^{-1}\boldsymbol{B}_{\text{ds}}^{\text{T}}\boldsymbol{\Upsilon}(\bar{\boldsymbol{x}}_m))\right\} \\ \boldsymbol{\Psi}_k^-(\bar{\boldsymbol{x}}) &= \underset{m,j}{\text{matrix}}\{\phi_j(\bar{\boldsymbol{x}}_m)\} \\ \boldsymbol{\Psi}_k^+(\bar{\boldsymbol{x}}) &= \underset{m,j}{\text{matrix}}\{\phi_j(\bar{\boldsymbol{x}}_m + \boldsymbol{B}_{\text{ds}}\boldsymbol{u}_{\text{ds},k}^*(\bar{\boldsymbol{x}}_m, t_k))\} \end{aligned} \tag{21}$$

C. Hybrid Nonlinear Optimal Control Law

Armed with the continuous-time and discrete-time optimal control gain equations [Eqs. (12) and (20), respectively], the desired hybrid nonlinear optimal control gains can be obtained via solving the following sets of equations (known as the hybrid optimal control gain equations) for $\boldsymbol{C}_N^*(t)$:

$$\begin{cases} \dot{\boldsymbol{C}}_N^*(t) + \boldsymbol{A}(t,c_{\text{k}}^*(t))\boldsymbol{C}_N^*(t) + \boldsymbol{b} = \boldsymbol{0}, \boldsymbol{C}_N^*(t_f) = \boldsymbol{0} \ \ [\text{See Eq. (13)}] & t \neq t_{\text{k}} \\ \boldsymbol{C}_N^*(t_{\text{k}}^-) = (\boldsymbol{\Psi}_k^-(\bar{\boldsymbol{x}}))^{-1}[\boldsymbol{W}_k(\bar{\boldsymbol{x}}) + \boldsymbol{\Psi}_k^+(\bar{\boldsymbol{x}})\boldsymbol{C}_N^*(t_k^+)] \ \ [\text{See Eq. (21)}] & t = t_{\text{k}} \end{cases} \tag{22}$$

Starting with the boundary conditions at the terminal time t_f, $\boldsymbol{C}_N^*(t_f) = \boldsymbol{0}$, the continuous-time optimal control gain equations are first integrated backward in time. At each jump instant $t = t_k$, an impulse is then induced in the solution using the discrete-time optimal control gain equations; and $\boldsymbol{C}_N^*(t_k^-)$ computed at each jump are subsequently used as new terminal conditions for the continuous-time equations in Eq. (22) to be integrated backward from t_k^- to t_{k-1}^+. This integration process is repeated until time zero is reached.

With the hybrid nonlinear optimal control gain vector thus computed at each time instant, the desired hybrid nonlinear optimal control law can be found by

$$\begin{cases} \boldsymbol{u}_{\text{ct}}^*(\boldsymbol{x},t) = -\frac{1}{2}\boldsymbol{R}_{\text{ct}}^{-1}\boldsymbol{g}^{\text{T}}(\boldsymbol{x},t)\mathbf{J}_{\boldsymbol{x}}^{\text{T}}(\boldsymbol{\Phi}_N(\boldsymbol{x}))\boldsymbol{C}_N^*(t) & t \neq t_k \\ \boldsymbol{u}_{\text{ds},k}^*(\boldsymbol{x}_k^+, t_k^+) = -\frac{1}{2}\boldsymbol{R}_{\text{ds}}^{-1}\boldsymbol{B}_{\text{ds}}^{\text{T}}\mathbf{J}_{\boldsymbol{x}}^{\text{T}}(\boldsymbol{\Phi}_N(\boldsymbol{x}))|_{\boldsymbol{x}=\boldsymbol{x}_k^+}\boldsymbol{C}_N^*(t_k^+) & t = t_k \end{cases} \tag{23}$$

Shown in Fig. 1, the proposed hybrid algorithm for nonlinear systems is compared to the hybrid linear quadratic regulator (LQR) approach applicable for linear systems [26], wherein $V(\boldsymbol{x}, t) \coloneqq \boldsymbol{x}^{\text{T}}\boldsymbol{P}(t)\boldsymbol{x}$.

III. Spacecraft Attitude Kinematics and Dynamics

As a hybrid dynamical system, the attitude control system proposed in this Note possesses two modes of operation: magnetic actuation and impulsive thrusting. In this regard, the spacecraft operating in a low-Earth orbit is externally torqued by three mutually perpendicular magnetic torquers immersed in the Earth's magnetic field. Once a certain criterion is met, a triple set of impulsive torques (one about each direction of the body-fixed frame) is then applied to the spacecraft by expulsion devices (thrusters). The attitude motion of the spacecraft is therefore characterized by a continuous-time set of differential equations, which characterizes the rotational motion of the dynamical system between impulsive events, and a set of difference equations, which governs instantaneous changes in the states once an impulse occurs. Due to the cascade nature of the spacecraft attitude motion, the rotational kinematic equations must be coupled with the dynamics. In this Note, the singularity-free four-parameter set of quaternions ($\boldsymbol{\varepsilon} = [\varepsilon_1 \quad \varepsilon_2 \quad \varepsilon_3]^{\text{T}}$ and η) subject to the unit magnitude constraint ($\boldsymbol{\varepsilon}^T\boldsymbol{\varepsilon} + \eta^2 = 1$) are chosen to parameterize

the attitude motion of the spacecraft. The kinematic equations of motion, which mathematically relate the angular velocity to the rate of change in quaternions, are therefore formulated as (Ref. [33] Chap. 2)

$$\begin{cases} \dot{\boldsymbol{\varepsilon}}(t) = (1/2)(\eta \mathbf{1}_{3\times 3} + \boldsymbol{\varepsilon}^{\times})\boldsymbol{\omega} \\ \dot{\eta}(t) = -(1/2)\boldsymbol{\varepsilon}^{T}\boldsymbol{\omega} \end{cases} \tag{24}$$

where $\boldsymbol{\omega}$ is the angular velocity, and $(\cdot)^{\times}$ denotes the skew-symmetric matrix used to implement the crossproduct. In addition, the rotational dynamics of the system are described by Euler's rigid-body equations [33]:

$$\boldsymbol{I}\dot{\boldsymbol{\omega}}(t) + \boldsymbol{\omega}^{\times}\boldsymbol{I}\boldsymbol{\omega} = \boldsymbol{\tau}_{\text{mag}} + \boldsymbol{\tau}_{\text{imp}} + \boldsymbol{\tau}_{\text{dist}} \tag{25}$$

wherein $\boldsymbol{I}$ is the spacecraft moment of inertia matrix. Furthermore, $\boldsymbol{\tau}_{\text{mag}}$ and $\boldsymbol{\tau}_{\text{imp}}$ define, respectively, the magnetic torques and impulsive thrusts applied at t_k; and they can be obtained by (Ref. [33] Chap. 9)

$$\boldsymbol{\tau}_{\text{mag}} = \boldsymbol{m}^{\times}\boldsymbol{B}_b \tag{26}$$

$$\boldsymbol{\tau}_{\text{imp}} = \sum_{k=1}^{N_{\text{imp}}} \boldsymbol{\nu}_k \delta(t - t_k) \tag{27}$$

wherein $\boldsymbol{m}$ is the commanded magnetic dipole moments generated by the magnetic torquers ($\boldsymbol{m} = \boldsymbol{u}_{\text{ct}}$), $\boldsymbol{B}_b$ specifies the local geomagnetic field expressed in the body-fixed coordinate system, $\boldsymbol{\nu}_k$ denotes impulsive torques produced by thrusters ($\boldsymbol{\nu}_k = \boldsymbol{u}_{\text{ds},k}$), and $\delta(t)$ is the Dirac delta function located at each impulse time $t = t_k$. In addition, external disturbance torques, which arise primarily from the gravity-gradient disturbances and residual magnetic dipoles resulting from onboard electronics, are the most significant source of disturbance for near-Earth small spacecraft; and they can be found as (Ref. [33] Chap. 9)

$$\boldsymbol{\tau}_{\text{dist}} = \frac{3\mu}{\|\boldsymbol{r}_b\|^5}\boldsymbol{r}_b^{\times}\boldsymbol{I}\boldsymbol{r}_b + \boldsymbol{m}_{\text{dist}}^{\times}\boldsymbol{B}_b \tag{28}$$

where $\mu = 3.986 \times 10^{14}\ \text{m}^3/\text{s}^2$ is the Earth's standard gravitational parameter, $\boldsymbol{r}_b$ is the spacecraft position vector in the body-fixed frame, and $\boldsymbol{m}_{\text{dist}}$ denotes the residual magnetic dipole moments. Furthermore, a nontilted dipole model of the geomagnetic field described in Ref. [34] is used in this Note to estimate the inertial magnetic field vector $\boldsymbol{B}_i$. The spacecraft magnetic/impulsive attitude control system can therefore be formulated as the following hybrid nonlinear dynamical system:

$$\begin{cases} \begin{cases} \dot{\boldsymbol{\varepsilon}}(t) = (1/2)(\eta \mathbf{1}_{3\times 3} + \boldsymbol{\varepsilon}^{\times})\boldsymbol{\omega} \\ \dot{\eta}(t) = -(1/2)\boldsymbol{\varepsilon}^{\text{T}}\boldsymbol{\omega} \\ \dot{\boldsymbol{\omega}}(t) = \boldsymbol{I}^{-1}(-\boldsymbol{\omega}^{\times}\boldsymbol{I}\boldsymbol{\omega} + \boldsymbol{\tau}_{\text{mag}} + \boldsymbol{\tau}_{\text{dist}}) \end{cases} & t \neq t_k \\ \Delta\boldsymbol{\omega}(t_k) = \boldsymbol{I}^{-1}\boldsymbol{\tau}_{\text{imp}} & t = t_k \end{cases} \tag{29}$$

IV. Numerical Simulations

In this section, the hybrid control design framework developed in Sec. II is exploited to detumble and point the spacecraft being considered immediately after launch. Due to the cascade nature of the spacecraft attitude control problem, the equations of motion given by Eq. (29) must be integrated simultaneously. To this end, Eq. (22) is first solved iteratively for the hybrid nonlinear optimal control gains $\boldsymbol{C}_N^*(t)$ used in both continuous-time and discrete-time optimal controllers. The hybrid rotational equations of motion, which take into account the external disturbance torques, are then integrated forward using a fixed-step fourth-order Runge–Kutta scheme (Ref. [30] Chap. 11).

Defining $\boldsymbol{x} = [\,\varepsilon_1 \quad \varepsilon_2 \quad \varepsilon_3 \quad \eta \quad \omega_1 \quad \omega_2 \quad \omega_3\,]^{\text{T}}$, the dynamic and control input functions can be obtained according to Eqs. (1) and (29) as follows:

$$\boldsymbol{f}(\boldsymbol{x}) = \begin{bmatrix} (1/2)(\eta \mathbf{1}_{3\times 3} + \boldsymbol{\varepsilon}^{\times})\boldsymbol{\omega} \\ -(1/2)\boldsymbol{\varepsilon}^{\text{T}}\boldsymbol{\omega} \\ -\boldsymbol{I}^{-1}\boldsymbol{\omega}^{\times}\boldsymbol{I}\boldsymbol{\omega} \end{bmatrix}, \qquad \boldsymbol{g}(\boldsymbol{\varepsilon}, \eta, t) = \begin{bmatrix} \mathbf{0}_{4\times 3} \\ -\boldsymbol{I}^{-1}\boldsymbol{B}_b^{\times} \end{bmatrix}$$

$$\boldsymbol{B}_{\text{ds}} = \begin{bmatrix} \mathbf{0}_{4\times 3} \\ \boldsymbol{I}^{-1} \end{bmatrix} \tag{30}$$

With $\boldsymbol{f}$, $\boldsymbol{g}$, and $\boldsymbol{B}_{\text{ds}}$ coming directly from the equations of motion, the domain of the states Ω, the basis functions $\boldsymbol{\Phi}_N$, the collocation points $\bar{\boldsymbol{x}}$, the impulsive application times $\boldsymbol{\theta}_k$, and the state penalty functions remain to be determined. Due to the unit magnitude constraint acting on the quaternions, their domain of possible values is thus limited to $[-1, 1]$. For angular velocity components, however, there is no kinematical limitation; their stability region is accordingly chosen on the basis of practical considerations (as expressed in radians per second):

$$\Omega = [-1 \quad 1]_{\varepsilon_1} \times [-1 \quad 1]_{\varepsilon_2} \times [-1 \quad 1]_{\varepsilon_3} \times [-1 \quad 1]_{\eta} \times [-1 \quad 1]_{\omega_1} \times [-1 \quad 1]_{\omega_2} \times [-1 \quad 1]_{\omega_3}$$

Proper selection of basis functions is critical to the design of the optimal controllers. For the control to compensate adequately for the nonlinear dynamics of the system, basis functions must be able to capture the essential nonlinear dynamics of the system. If the system has dynamics that are not spanned by the basis functions, then the control will not be able to compensate for the nonlinear dynamics of the system (characteristic requirement) [32,35]. The number of the basis elements must also be sufficiently large to approximate V_N with sufficient accuracy (quantity requirement) [32,35]. Due to multiplication of $\boldsymbol{g}^{\text{T}}(\boldsymbol{x}, t)$ and $\mathbf{J}_{\boldsymbol{x}}^{\text{T}}(\boldsymbol{\Phi}_N(\boldsymbol{x}))$ in the continuous-time optimal control law [Eq. (14)], basis functions must be selected such that their partial derivatives with respect to those states that correspond to nonzero elements of $\boldsymbol{g}$ result in desired functions of the states to ultimately emerge in the optimal control law, hence capturing the dominant nonlinear dynamics of the system.

Considering the structure of $\boldsymbol{g}(\boldsymbol{x}, t)$ for the magnetic attitude control problem, ω_1, ω_2, and ω_3 are those states that correspond to the nonzero elements of $\boldsymbol{g}$ in Eq. (14) as shown in the following:

$$\boldsymbol{u}_{\text{ct}}^*(\boldsymbol{x}, t) = -\frac{1}{2}\boldsymbol{R}_{\text{ct}}^{-1}\begin{bmatrix} 0 & 0 & 0 & 0 & 0 & g_{61} & g_{71} \\ 0 & 0 & 0 & 0 & g_{52} & 0 & g_{72} \\ 0 & 0 & 0 & 0 & g_{53} & g_{63} & 0 \end{bmatrix}\begin{bmatrix} \dfrac{\partial\phi_1}{\partial\varepsilon_1} & \cdots & \dfrac{\partial\phi_N}{\partial\varepsilon_1} \\ \vdots & & \vdots \\ \dfrac{\partial\phi_1}{\partial\omega_3} & \cdots & \dfrac{\partial\phi_N}{\partial\omega_3} \end{bmatrix} \times \begin{bmatrix} c_1^*(t) \\ \vdots \\ c_N^*(t) \end{bmatrix}$$

$$= -\frac{1}{2}\boldsymbol{R}_{\text{ct}}^{-1}\begin{bmatrix} g_{61}\dfrac{\partial\phi_1}{\partial\omega_2} + g_{71}\dfrac{\partial\phi_1}{\partial\omega_3} & \cdots & g_{61}\dfrac{\partial\phi_N}{\partial\omega_2} + g_{71}\dfrac{\partial\phi_N}{\partial\omega_3} \\ g_{52}\dfrac{\partial\phi_1}{\partial\omega_1} + g_{72}\dfrac{\partial\phi_1}{\partial\omega_3} & \cdots & g_{52}\dfrac{\partial\phi_N}{\partial\omega_1} + g_{72}\dfrac{\partial\phi_N}{\partial\omega_3} \\ g_{53}\dfrac{\partial\phi_1}{\partial\omega_1} + g_{63}\dfrac{\partial\phi_1}{\partial\omega_2} & \cdots & g_{53}\dfrac{\partial\phi_N}{\partial\omega_1} + g_{63}\dfrac{\partial\phi_N}{\partial\omega_2} \end{bmatrix} \times \begin{bmatrix} c_1^*(t) \\ \vdots \\ c_N^*(t) \end{bmatrix}$$

wherein g_{52}, g_{53}, g_{61}, g_{63}, g_{71}, and g_{72} represent nonzero elements of $\boldsymbol{g}(\boldsymbol{x}, t)$. With an attitude controller composed of quaternion-based

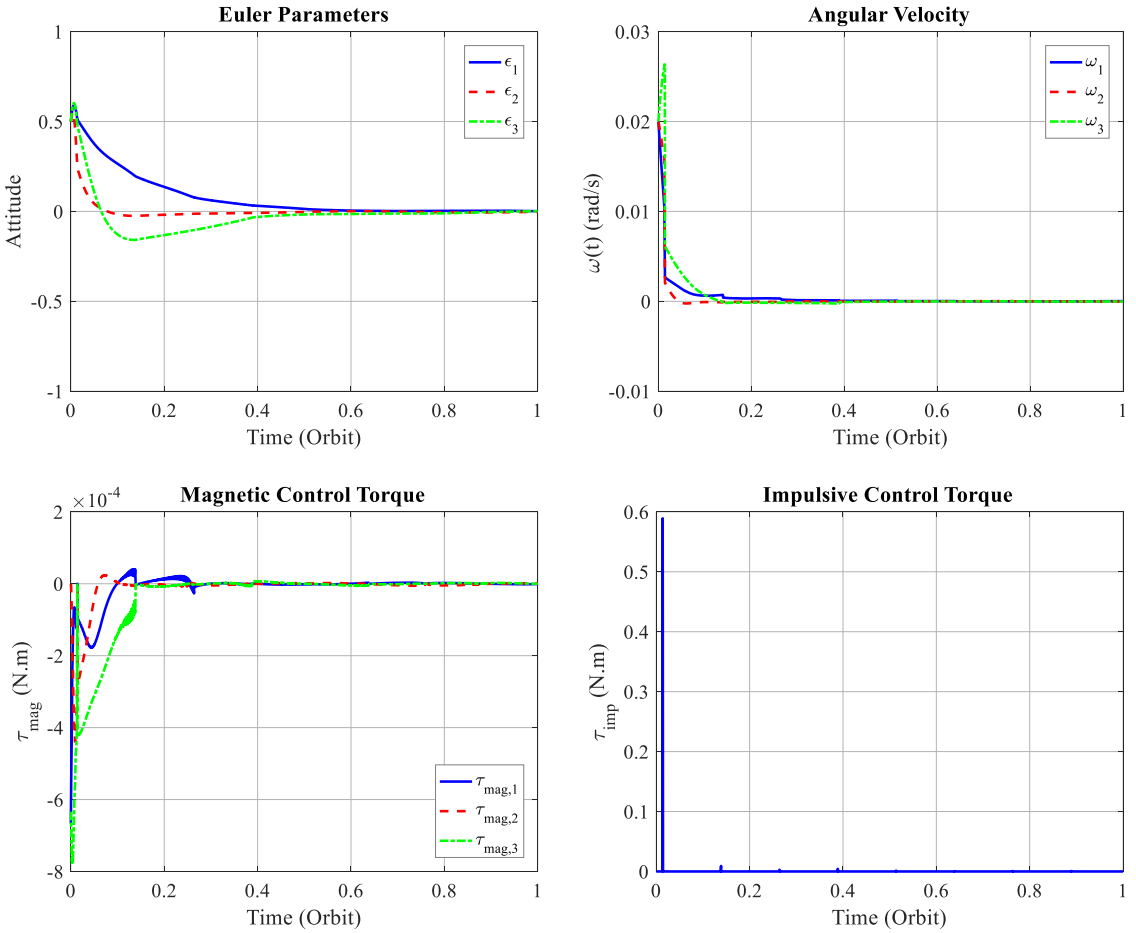

Fig. 2 Time histories of Euler parameters, angular velocity, and control torques for the proposed hybrid nonlinear optimal controller using $\boldsymbol{\varepsilon}_0 = [0.5 \quad 0.5 \quad 0.5]^{\mathrm{T}}$ and $\boldsymbol{\omega}_0 = [0.02 \quad 0.02 \quad 0.02]^{\mathrm{T}}$ rad/s.

proportional and $\boldsymbol{\omega}$-based rate control portions in mind, an initial set of quadratic basis elements are first chosen to satisfy the characteristic requirement: $\{\varepsilon_1\omega_1, \omega_1^2, \varepsilon_2\omega_2, \omega_2^2, \varepsilon_3\omega_3, \omega_3^2\}$. This choice must be, however, complemented by $\{\varepsilon_1^2, \varepsilon_2^2, \varepsilon_3^2, (\eta-1)^2\}$ to produce a positive-definite value function (Lyapunov function). Through this quadratic choice, the characteristic requirement is accordingly satisfied, and the asymptotic stability may be achieved. Nevertheless, these quadratic basis elements must be augmented by some extra higher-order terms to guarantee the accuracy of the approximation in addition to improving the performance of the optimal controller. By gradual increase in the number of basis elements in a manner consistent with the characteristic requirement, the performance index is eventually converged at $N = 28$ (i.e., $V_{N=28} \cong V$) and the quantity requirement is accordingly met. Henceforth, any further increase in the number of basis elements yields insignificant improvement in the performance index at the expense of computational cost. Considering these guidelines, the following 28 basis elements are consequently chosen for this problem:

$$\begin{aligned}\boldsymbol{\Phi}_{\mathrm{N}} = \{&\varepsilon_1^2, \varepsilon_1\omega_1, \omega_1^2, \varepsilon_2^2, \varepsilon_2\omega_2, \omega_2^2, \varepsilon_3^2, \varepsilon_3\omega_3, \omega_3^2, (\eta-1)^2,\\ &\varepsilon_1^4, \varepsilon_1^2\omega_1^2, \omega_1^4, \varepsilon_2^4, \varepsilon_2^2\omega_2^2, \omega_2^4, \varepsilon_3^4, \varepsilon_3^2\omega_3^2, \omega_3^4,\\ &\varepsilon_1^4\omega_1^2, \varepsilon_2^4\omega_2^2, \varepsilon_3^4\omega_3^2, \varepsilon_1^7\omega_1, \varepsilon_2^7\omega_2, \varepsilon_3^7\omega_3, \varepsilon_1^5\omega_1^3, \varepsilon_2^5\omega_2^3, \varepsilon_3^5\omega_3^3\}\end{aligned}$$

A suitable set of collocation points is also necessary to design the discrete-time optimal controller. Collocation points can be chosen from the entire compact set, excluding the origin, provided the rank condition required to produce an invertible $\boldsymbol{\Psi}_k^-(\bar{\boldsymbol{x}})$ in Eq. (20) is satisfied (see section 3 in Ref. [27] for a detailed discussion).

Assuming a prescribed sequence of impulsive times, eight equally spaced impulses in terms of true anomaly are selected for this problem:

$$\begin{aligned}\boldsymbol{\theta}_k = \{&5\ \mathrm{deg}, 50\ \mathrm{deg}, 95\ \mathrm{deg}, 140\ \mathrm{deg}, 185\ \mathrm{deg},\\ &230\ \mathrm{deg}, 275\ \mathrm{deg}, 320\ \mathrm{deg}\}\end{aligned}$$

This choice suggests the firing times through which a minimum value for J is obtained. In addition, consistent with the LQR approach, the state penalty functions in this Note are chosen to be quadratic: $l_{\mathrm{ct}}(\boldsymbol{x}) = \boldsymbol{x}^{\mathrm{T}}\boldsymbol{Q}_{\mathrm{ct}}\boldsymbol{x}$ and $l_{\mathrm{ds}}(\boldsymbol{x}_k^-) = \boldsymbol{x}_k^{-\mathrm{T}}\boldsymbol{Q}_{\mathrm{ds}}\boldsymbol{x}_k^-$, where $\boldsymbol{Q}_{\mathrm{ct}}$ and $\boldsymbol{Q}_{\mathrm{ds}}$ are symmetric positive semidefinite matrices called the continuous-time and discrete-time state penalty matrices, respectively.

Assuming a circular near-polar Keplerian orbit, the spacecraft orbital elements with the semimajor axis a corresponding to the altitude of 450 km are defined as

$$\{a, e, \hat{i}, \hat{\Omega}, \hat{\omega}, t_0\} = \{6828\ \mathrm{km}, 0,87\ \ \mathrm{deg}, 0\ \ \mathrm{deg}, 0\ \ \mathrm{deg}, 0\}$$

where e, $\hat{i}$, $\hat{\Omega}$, and $\hat{\omega}$ are the eccentricity, inclination, right ascension of the ascending node, and argument of perigee, respectively. In addition, the following weighting matrices are selected for trading off the speed of the response against the control effort, and hence produce the satisfactory performance:

$$\begin{aligned}\boldsymbol{Q}_{\mathrm{ct}} &= \mathrm{diag}(\,10 \quad 10 \quad 10 \quad 0 \quad 1 \quad 1 \quad 1\,),\\ \boldsymbol{R}_{\mathrm{ct}} &= \mathrm{diag}(\,10^{-7} \quad 10^{-7} \quad 10^{-7}\,)\\ \boldsymbol{Q}_{\mathrm{ds}} &= \mathrm{diag}(\,10 \quad 10 \quad 10 \quad 0 \quad 1 \quad 1 \quad 1\,),\\ \boldsymbol{R}_{\mathrm{ds}} &= \mathrm{diag}(\,14\times10^{-2} \quad 14\times10^{-2} \quad 14\times10^{-2}\,)\end{aligned}$$

As seen, the diagonal term associated with η is chosen to be zero for both continuous-time and discrete-time state penalty matrices. The objective here is to regulate the states ε_1, ε_2, ε_3, ω_1, ω_2, and ω_3, leaving η to vary as necessary to control the attitude motion of spacecraft appropriately while satisfying the unit length constraint: $\boldsymbol{\varepsilon}^{\mathrm{T}}\boldsymbol{\varepsilon} + \eta^2 = 1$.

Lastly, the spacecraft is assumed to have $\boldsymbol{I} = \mathrm{diag}(27 \;\; 17 \;\; 25)$ $\mathrm{kg}\cdot\mathrm{m}^2$ with residual magnetic dipole moments of $\boldsymbol{m}_{\mathrm{dist}} = [\,0.1 \quad 0.1 \quad 0.1\,]^{\mathrm{T}}$ $\mathrm{A}\cdot\mathrm{m}^2$.

As demonstrated in Ref. [26], a hybrid (magnetic/impulsive) LQR controller initialized by a sufficiently small set of initial conditions (namely, $\boldsymbol{\varepsilon}_0 = [\,0 \quad 0 \quad 0\,]^{\mathrm{T}}$ and $\boldsymbol{\omega}_0 = [\,0.02 \quad 0.02 \quad 0.02\,]^{\mathrm{T}}$ rad/s) can asymptotically stabilize the attitude motion of the spacecraft. This undemanding attempt is eliminated in this Note, and the system is challenged by a large set of initial rotation $\boldsymbol{\varepsilon}_0 = [\,0.5 \quad 0.5 \quad 0.5\,]^{\mathrm{T}}$. The simulation results are shown in Fig. 2. As seen, the transient response of the system is reasonably quick and well damped, and the system is stable after one orbit.

To evaluate the performance of the hybrid nonlinear optimal controller developed in Sec. II, a hybrid LQR controller [26] and a magnetic nonlinear optimal controller [36] are also designed. The former is based on the linearized rotational equations of motion; whereas the latter, which only uses the continuous-time magnetic actuation (without impulsive thrusts), is designed using the full nonlinear kinematics and dynamics of the system. In addition, the following root-mean-square norms are defined and computed over 10 orbits to quantitatively assess the functionality of the proposed controller as opposed to the other two:

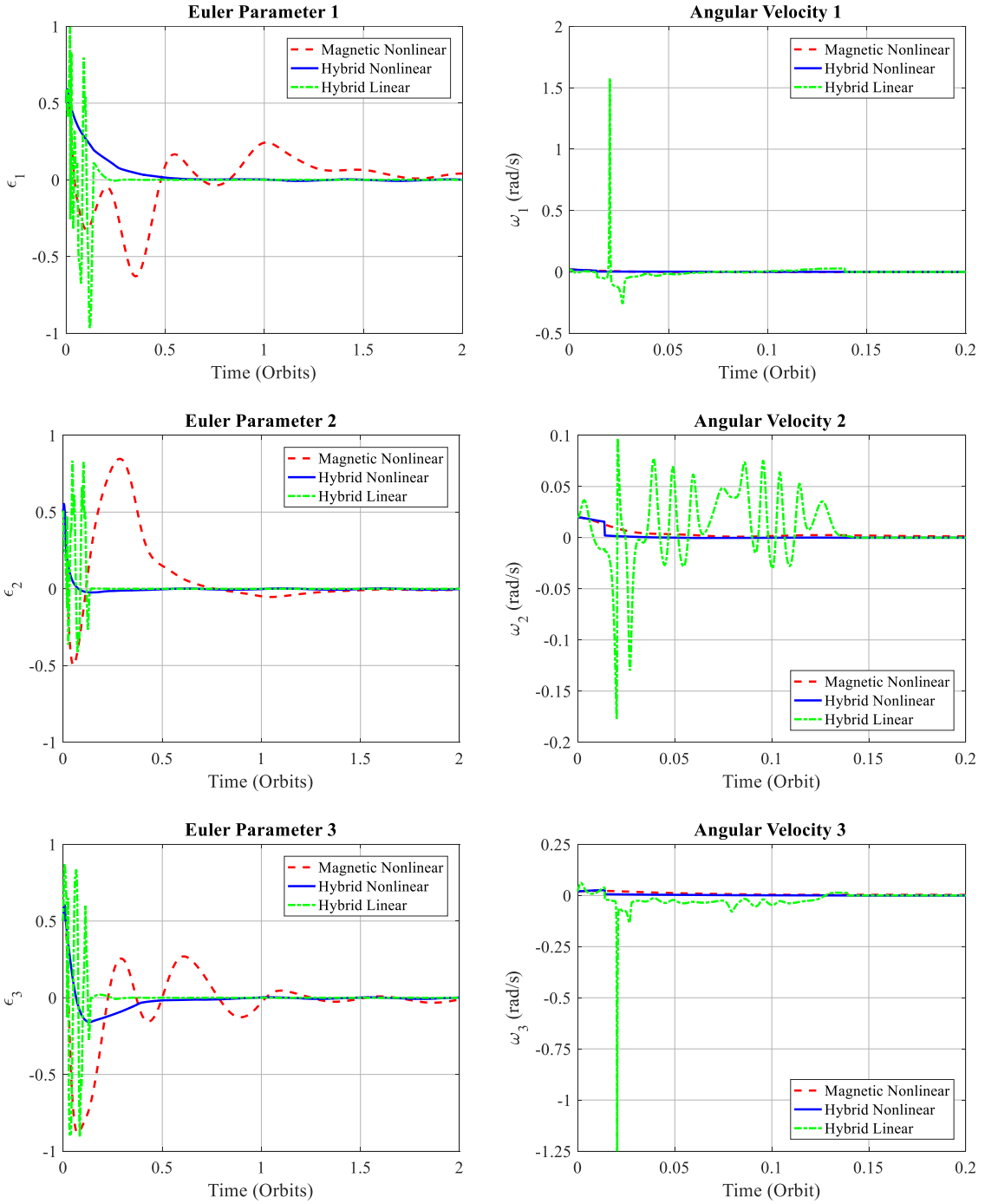

Fig. 3 Time histories of Euler parameters (left column) and angular velocity (right column) for the three optimal attitude controllers using $\boldsymbol{\varepsilon}_0 = [\,0.5 \quad 0.5 \quad 0.5\,]^{\mathrm{T}}$ and $\boldsymbol{\omega}_0 = [\,0.02 \quad 0.02 \quad 0.02\,]^{\mathrm{T}}$ rad/s.

$$\overline{\|\phi\|} = \sqrt{\frac{\int_0^{10T} \phi^2 \, \mathrm{d}t}{10T}}, \qquad \overline{\|\boldsymbol{\omega}\|} = \sqrt{\frac{\int_0^{10T} \boldsymbol{\omega}^{\mathrm{T}}\boldsymbol{\omega} \, \mathrm{d}t}{10T}},$$

$$\overline{\|\boldsymbol{\tau}_{\mathrm{mag}}\|} = \sqrt{\frac{\int_0^{10T} \boldsymbol{\tau}_{\mathrm{mag}}^{\mathrm{T}}\boldsymbol{\tau}_{\mathrm{mag}} \, \mathrm{d}t}{10T}}, \qquad \overline{\|\boldsymbol{\tau}_{\mathrm{imp}}\|} = \sqrt{\frac{\sum_{k=0}^{N_{\mathrm{imp}}} (\boldsymbol{u}_{\mathrm{ds},k}^{*\mathrm{T}}\boldsymbol{u}_{\mathrm{ds},k}^{*})}{N_{\mathrm{imp}}}}$$

where T is the orbital period, and ϕ denotes the rotation angle (in radians) of the spacecraft from Euler axis-angle parameters. In this regard, the norms of the rotation angle and impulsive torque ($\overline{\|\phi\|}$ and $\overline{\|\boldsymbol{\tau}_{\mathrm{imp}}\|}$, respectively) can be used as important criteria for accurate pointing and efficient fuel missions, respectively. By adjusting the size of the diagonal terms in weighting matrices, a tradeoff between accuracy and fuel expenditure can be made to achieve a high-precision pointing with low fuel requirements. Furthermore, the norm of the magnetic torque $\overline{\|\boldsymbol{\tau}_{\mathrm{mag}}\|}$ can be employed to evaluate the feasibility of the attitude controller in terms of the magnetic torque required by torque rods for stabilization purposes.

One important factor to determine the feasibility of a control scheme proposed for regulating the attitude motion of spacecraft is the required power during the mission. Assuming the spacecraft being considered is equipped with three magnetic torquers with $\mathcal{R} = 100\ \Omega, \mathcal{N} = 400$ turns, and $\mathcal{A} = \pi\mathcal{D}^2/4\ \mathrm{m}^2$ [1]; the electrical energy consumed by the spacecraft during the operating time can be estimated by [1]

$$E = \frac{3\mathcal{R}}{\mathcal{N}^2\mathcal{A}^2}\int_{t_0}^{t_f} \boldsymbol{m}^{\mathrm{T}}\boldsymbol{m} \, \mathrm{d}t$$

Whereas linear-based controllers are essentially restricted to operate in the vicinity of the equilibrium to satisfy the linearity assumption, the control systems equipped with nonlinear-based controllers can be employed to operate over the entire operating range of the system. Figure 3 depicts the time histories of Euler parameters and the angular velocity for the proposed hybrid nonlinear controller as opposed to the other two controllers starting from the same initial conditions. As is evident, the results show significant improvement in terms of transient response and settling time for the hybrid nonlinear controller as compared to the hybrid LQR and magnetic nonlinear controllers. In this regard, the hybrid LQR controller obtains comparatively good performance at the expense of large control effort; this occurs because the control used in the performance index is the linearized control, and not the actual one.

Presented in Table 1, all quantitative parameters related to the three attitude controllers are summarized. As seen, noticeable improvement in all parameters associated with the hybrid nonlinear controller is evident as compared to the other two; particularly J and E with 99.79 and 100.00% improvement, respectively. Whereas the magnetic torque required by the proposed controller for detumbling the spacecraft is only 7.81×10^{-5} N · m associated with $\boldsymbol{m} = 2.92$ A · m^2 over 10 orbits, and therefore lies within the acceptable range of 10^{-5} to 10^{-4} N · m as proposed in Refs. [2,3] for near-Earth missions, the hybrid LQR controller needs torque rods capable of 24, 164 A · m^2 at the expense of an inevitable increase in the dimensions and weight of the attitude control system (via increasing $\mathcal{N}$ and $\mathcal{A}$), which is obviously impossible in practice.

As stressed earlier, the hybrid LQR controller possesses a local asymptotic stability property within the linearity assumption, and therefore works well only for sufficiently small initial conditions; by choosing large initial rotation, asymptotic stabilization is obtained at the cost of large, practically impossible, magnetic torques. Moreover, once the system is initialized by a larger set of angular velocities, the hybrid LQR controller fails to stabilize appropriately (see Fig. 4). In contrast, no matter how large the initial angular velocity is chosen, the hybrid nonlinear controller can asymptotically stabilize the system

Table 1 Quantitative assessment for the performance of three optimal attitude controllers over 10 orbits using $\boldsymbol{\varepsilon}_0 = [0.5 \quad 0.5 \quad 0.5]^{\mathrm{T}}$ and $\boldsymbol{\omega}_0 = [0.02 \quad 0.02 \quad 0.02]^{\mathrm{T}}$ rad/s

Parameters	Hybrid linear (I)	Magnetic nonlinear (II)	Hybrid nonlinear (III)	Improvement of III as compared to I, %	Improvement of III as compared to II, %
J	9.88×10^5	1.78×10^4	2.11×10^3	99.79	88.22
E, J	2.98×10^{18}	5.66×10^{11}	4.35×10^{10}	100.00	92.31
$\overline{\|\phi\|}$, rad	4.88×10^{-1}	8.10×10^{-1}	2.57×10^{-1}	47.39	68.34
$\overline{\|\boldsymbol{\omega}\|}$, rad/ sec	2.28×10^{-2}	3.45×10^{-3}	2.36×10^{-3}	89.65	31.49
$\overline{\|\boldsymbol{\tau}_{\mathrm{mag}}\|}$, N · m	4.20×10^{-1}	2.81×10^{-4}	7.81×10^{-5}	99.98	72.23
$\overline{\|\boldsymbol{\tau}_{\mathrm{imp}}\|}$, N · m	4.22×10^{-1}	— —	1.20×10^{-1}	71.50	— —

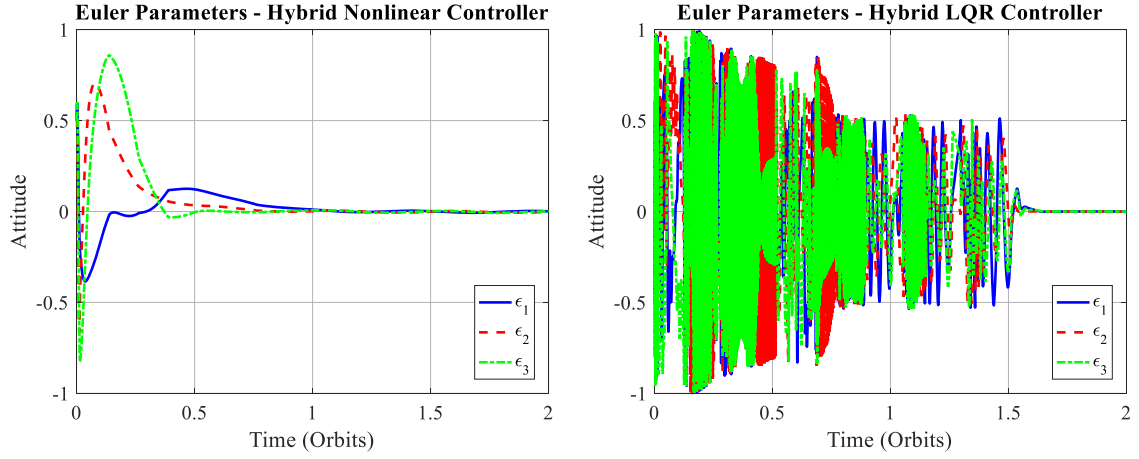

Fig. 4 Time histories of Euler parameters for hybrid nonlinear optimal controller (left) and hybrid LQR controller (right) using $\boldsymbol{\varepsilon}_0 = [0.5 \quad 0.5 \quad 0.5]^{\mathrm{T}}$ and $\boldsymbol{\omega}_0 = [0.06 \quad 0.06 \quad 0.06]^{\mathrm{T}}$ rad/s.

accordingly. Figure 4 shows the time history of the Euler parameters for two hybrid optimal attitude controllers using a slightly larger set of initial angular velocities: $\boldsymbol{\omega}_0 = [0.06\ 0.06\ 0.06]^{\mathrm{T}}$ rad/s. As seen, the proposed controller can still regulate the spacecraft attitude motion appropriately, and hence the global asymptotic stability from a practical perspective. In this regard, the domain of the states associated with $\boldsymbol{\omega}$ in Ω can be expanded unboundedly, depending upon the practical considerations.

V. Conclusions

In this Note, a novel hybrid control scheme has been proposed for regulating the attitude motion of spacecraft. The proposed algorithm combined magnetic torques with impulsive thrusts in an optimal manner. Assuming a prescribed set of impulsive application times, a nonlinear optimal approach was exploited to determine the control input that minimized the hybrid performance index being considered. By using the proposed hybrid nonlinear optimal controller, three objectives have been accomplished in this Note:

1) Instantaneous underactuation and gain limitations (as the two main obstacles inherently associated with magnetically actuated attitude control systems) were resolved.

2) Global asymptotic stability for the hybrid controller was shown from a practical perspective.

3) The quantitative parameters characterizing the performance of the hybrid control system were significantly improved as compared to the hybrid LQR and nonlinear magnetic controllers.

Numerical simulation results showed the feasibility of the proposed controller with magnetotorquers requiring magnetic torques within the acceptable range of 10^{-5} to 10^{-4} N · m for stabilizing the attitude motion of the spacecraft under consideration.

References

[1] Wertz, J. R., *Spacecraft Attitude Determination and Control*, D. Reidel Publishing, Dordrecht, The Netherlands, 1978, Chap. 5.

[2] Sidi, M. J., *Spacecraft Dynamics and Control: A Practical Engineering Approach*, Cambridge Univ. Press, Cambridge, England, U.K., 1997, Chap. 7.

[3] Markley, F. L., and Crassidis, J. L., *Fundamentals of Spacecraft Attitude Determination and Control*, Springer, New York, 2014, Chap. 7.

[4] Avanzini, G., and Giulietti, F., "Magnetic Detumbling of a Rigid Spacecraft," *Journal of Guidance, Control, and Dynamics*, Vol. 35, No. 4, July–Aug. 2012, pp. 1326–1334. https://doi.org/10.2514/1.53074

[5] Camillo, P. J., and Markley, F. L., "Orbit-Averaged Behavior of Magnetic Control Laws for Momentum Unloading," *Journal of Guidance, Control, and Dynamics*, Vol. 3, No. 6, 1980, pp. 563–568. https://doi.org/10.2514/3.19725

[6] Lovera, M., "Optimal Magnetic Momentum Control for Inertially Pointing Spacecraft," *European Journal of Control*, Vol. 7, No. 1, 2001, pp. 30–39. https://doi.org/10.1016/S0947-3580(01)70936-3

[7] White, J. S., Shigemoto, F. H., and Bourquin, K., "Satellite Attitude Control Utilizing the Earth's Magnetic Field," NASA TN-D-1068, A-474, 1961.

[8] Stickler, A. C., and Alfriend, K. T., "Elementary Magnetic Attitude Control System," *Journal of Spacecraft and Rockets*, Vol. 13, No. 5, 1976, pp. 282–287. https://doi.org/10.2514/3.57089

[9] Martel, F., Pal, P. K., and Psiaki, M., "Active Magnetic Control System for Gravity Gradient Stabilized Spacecraft," *Proceedings of the 2nd Annual AIAA/USU Conference on Small Satellites*, AIAA, Washington, D.C., 1988, pp. 1–19.

[10] Arduini, C., and Baiocco, P., "Active Magnetic Damping Attitude Control for Gravity-Gradient Stabilized Spacecraft," *Journal of Guidance, Control, and Dynamics*, Vol. 20, No. 1, Jan.–Feb. 1997, pp. 117–122. https://doi.org/10.2514/2.4003

[11] Wiśniewski, R., "Linear Time-Varying Approach to Satellite Attitude Control Using Only Electromagnetic Actuation," *Journal of Guidance, Control, and Dynamics*, Vol. 23, No. 4, July–Aug. 2000, pp. 640–647. https://doi.org/10.2514/2.4609

[12] Psiaki, M. L., "Magnetic Torquer Attitude Control via Asymptotic Periodic Linear Quadratic Regulation," *Journal of Guidance, Control, and Dynamics*, Vol. 24, No. 2, March–April 2001, pp. 386–394. https://doi.org/10.2514/2.4723

[13] Lovera, M., de Marchi, E., and Bittanti, S., "Periodic Attitude Control Techniques for Small Satellites with Magnetic Actuators," *IEEE Transactions on Control Systems Technology*, Vol. 10, No. 1, Jan. 2002, pp. 90–95. https://doi.org/10.1109/87.974341

[14] Wiśniewski, R., and Blanke, M., "Fully Magnetic Attitude Control for Spacecraft Subject to Gravity Gradient," *Automatica*, Vol. 35, No. 7, July 1999, pp. 1201–1214. https://doi.org/10.1016/S0005-1098(99)00021-7

[15] Damaren, C. J., "Comments on "Fully Magnetic Attitude Control for Spacecraft Subject to Gravity Gradient"," *Automatica*, Vol. 38, No. 12, Dec. 2002, pp. 2189–2189. https://doi.org/10.1016/S0005-1098(02)00146-2

[16] Silani, E., and Lovera, M., "Magnetic Spacecraft Attitude Control: A Survey and Some New Results," *Control Engineering Practice*, Vol. 13, No. 3, March 2005, pp. 357–371. https://doi.org/10.1016/j.conengprac.2003.12.017

[17] Bhat, S. P., and Dham, A. S., "Controllability of Spacecraft Attitude Under Magnetic Actuation," *Proceedings of the 42nd IEEE Conference on Decision and Control*, IEEE Publ., Piscataway, NJ, 2003, pp. 2383–2388. https://doi.org/10.1109/cdc.2003.1272976

[18] Hecht, E., and Manger, W. P., "Magnetic Attitude Control of the Tiros Satellites," *Applied Mathematics and Mechanics*, Vol. 7, 1964, pp. 127–135. https://doi.org/10.1016/B978-0-12-395776-4.50014-8

[19] Parkinson, B. W., and Kasdin, N. J., "A Magnetic Attitude Control System for Precision Pointing of the Rolling GP-B Spacecraft," *Acta Astronautica*, Vol. 21, Nos. 6–7, 1990, pp. 477–486. https://doi.org/10.1016/0094-5765(90)90065-S

[20] Lovera, M., and Astolfi, A., "Global Magnetic Attitude Control of Spacecraft in the Presence of Gravity-Gradient," *IEEE Transactions on Aerospace and Electronic Systems*, Vol. 42, No. 3, July 2006, pp. 796–805. https://doi.org/10.1109/TAES.2006.248214

[21] Hablani, H. B., "Comparative Stability Analysis and Performance of Magnetic Controllers for Bias Momentum Satellites," *Journal of Guidance, Control, and Dynamics*, Vol. 18, No. 6, Nov.–Dec. 1995, pp. 1313–1320. https://doi.org/10.2514/3.21547

[22] Damaren, C. J., "Hybrid Magnetic Attitude Control Gain Selection," *Journal of Aerospace Engineering*, Vol. 223, No. 8, Aug. 2009, pp. 1041–1047. https://doi.org/10.1243/09544100 JAERO641

[23] Forbes, J. R., and Damaren, C. J., "Geometric Approach to Spacecraft Attitude Control Using Magnetic and Mechanical Actuation," *Journal of Guidance, Control, and Dynamics*, Vol. 33, No. 2, March–April 2010, pp. 590–595. https://doi.org/10.2514/1.46441

[24] Forbes, J. R., and Damaren, C. J., "Linear Time-Varying Passivity-Based Attitude Control Employing Magnetic and Mechanical Actuation," *Journal of Guidance, Control, and Dynamics*, Vol. 34, No. 5, Sept.–Oct. 2011, pp. 1363–1372. https://doi.org/10.2514/1.51899

[25] Pulecchi, T., and Lovera, M., "Attitude Control of Spacecraft with Partially Magnetic Actuation," *IFAC Proceedings Volumes*, Vol. 40, No. 7, 2007, pp. 609–614. https://doi.org/10.3182/20070625-5-FR-2916.00104

[26] Vatankhahghadim, B., and Damaren, C. J., "Optimal Combination of Magnetic Attitude Control with Impulsive Thrusting," *Journal of Guidance, Control, and Dynamics*, Vol. 39, No. 10, Oct. 2016, pp. 2391–2398. https://doi.org/10.2514/1.G001664

[27] Sharifi, E., and Damaren, C. J., "A Numerical Approach to Hybrid Nonlinear Optimal Control," *International Journal of Control*, (to be published).

[28] Haddad, W. M., Chellaboina, V., and Kablar, N. A., "Nonlinear Impulsive Dynamical Systems. Part II: Stability of Feedback Interconnections and Optimality," *International Journal of Control*, Vol. 74, No. 17, 2001, pp. 1659–1677. https://doi.org/10.1080/00207170110080959

[29] Fletcher, C. A. J., *Computational Galerkin Methods*, Springer Series in Computational Physics, Springer, New York, 1984.

[30] Quarteroni, A., Sacco, R., and Saleri, F., *Numerical Mathematics*, Springer–Verlag, New York, 2000.

[31] Haddad, W. M., and Chellaboina, V., *Nonlinear Dynamical Systems and Control: A Lyapunov-Based Approach*, Princeton Univ. Press, Princeton, NJ, 2008.

[32] Beard, R., "Improving the Closed-Loop Performance of Nonlinear Systems," Ph.D. Dissertation, Rensselaer Polytechnic Inst., Troy, New York, 1995.
[33] Hughes, P. C., *Spacecraft Attitude Dynamics*, Wiley, New York, 1986.
[34] Yamakawa, H., Bando, M., Yano, K., and Tsujii, S., "Spacecraft Relative Dynamics Under the Influence of the Geomagnetic Lorentz Force," *AIAA Guidance, Navigation and Control Conference*, AIAA Paper 2010-8128, 2010. https://doi.org/10.2514/6.2010-8128
[35] Beard, R., Saridis, G., and Wen, J., "Improving the Performance of Stabilizing Controls for Nonlinear Systems," *IEEE Control Systems Magazine*, Vol. 16, No. 5, Oct. 1996, pp. 27–35. https://doi.org/10.1109/37.537206
[36] Sharifi, E., and Damaren, C. J., "Nonlinear Optimal Approach to Magnetic Spacecraft Attitude Control," *AIAA Guidance, Navigation and Control Conference*, AIAA Paper 2020-1105, 2020. https://doi.org/10.2514/6.2020-1105